

1 **Revision 1**

2

3 Compositional zoning in dolomite from lawsonite-bearing eclogite (SW Tianshan, China):

4 Evidence for prograde metamorphism during subduction of oceanic crust

5

6 Ji-Lei Li,^{1,*} Reiner Klemd,¹ Jun Gao,² and Melanie Meyer¹

7

8 ¹*GeoZentrum Nordbayern, Universität Erlangen–Nürnberg, Schlossgarten 5a, D-91054*

9 *Erlangen, Germany*

10 ²*Key Laboratory of Mineral Resources, Institute of Geology and Geophysics, Chinese*

11 *Academy of Sciences, P.O. Box 9825, Beijing 100029, China*

12

13 *Present address: GeoZentrum Nordbayern, Universität Erlangen–Nürnberg, Schlossgarten 5a,

14 D-91054 Erlangen, Germany. E-mail: jilei.li@gzn.uni-erlangen.de

15

16

ABSTRACT

17 Dolomite with compositional zoning was discovered in carbonate-lawsonite-bearing eclogites
18 in the Tianshan (ultra-)high-pressure/low-temperature metamorphic belt, northwestern China.
19 The eclogite-facies dolomite occurs as matrix porphyroblast and as inclusion in garnet, both
20 of which display the same chemical zoning pattern. The dolomite contains inclusions of
21 calcite (probably after aragonite), magnesite, glaucophane, lawsonite (and its pseudomorphs),
22 allanite, epidote, paragonite, phengite and omphacite. The chemical zoning in dolomite is
23 well defined by a continuous core-to-rim Mg increase and Fe-Mn decrease. The
24 concentrations of transition metal elements, REE and Y also decrease from core to rim of the
25 dolomite. Thermodynamic modeling demonstrates that the Fe-Mg zoning of dolomite is
26 largely temperature dependent and, thus, is interpreted as prograde growth zoning, which
27 developed during subduction of carbonate-bearing oceanic crust. It is suggested that dolomite
28 in equilibrium with garnet formed as a result of changing matrix compositions due to
29 increasing temperatures. In addition, thermodynamic modeling demonstrates that during
30 subduction at high-pressure conditions prograde-formed aragonite and dolomite were
31 transformed to dolomite and magnesite. Furthermore, Fe-rich magnesite inclusions in matrix
32 dolomite and in dolomite inclusions in garnet are shown to have formed during high-pressure
33 conditions prior to peak metamorphic conditions and, therefore caution is warranted using
34 Fe-bearing magnesite occurrences in eclogite-facies rocks as an unambiguous ultrahigh
35 pressure indicator as previously suggested.

36 **Keywords:** prograde zoning, dolomite, magnesite, eclogite, high pressure, Tianshan

37

38

39

INTRODUCTION

40 Carbonates are common minerals in some blueschists and eclogites in (ultra-)high-
41 pressure/low-temperature ((U)HP/LT) metamorphic terranes. Coesite inclusions in dolomite
42 in eclogite-facies calc-silicate rocks and metabasalts from the Dabie ultrahigh-pressure (UHP)
43 belt were interpreted as evidence for the subduction of continental crust (including sediments)
44 to mantle depths (>100 km) and that coexisting dolomite and magnesite are stable mineral
45 phases under UHP conditions (Schertl and Okay 1994; Zhang and Liou 1996). Coexisting
46 magnesite, aragonite and calcite inclusions in dolomite have also been reported to occur in
47 eclogites from several high-pressure (HP) and UHP metamorphic terranes and are regarded to
48 be an UHP indicator (e.g., Wang and Liou 1993; Zhang and Liou 1994; Zhang et al. 2003).
49 However, the coexistence of magnesite and dolomite as well as magnesite inclusions in
50 dolomite in blueschists and eclogites were also interpreted to have formed under HP
51 conditions (e.g., Klemd 2003; Smit et al. 2008; Li et al. 2012).

52 Compositional zoning is a distinctive feature that is commonly observed in petrographical
53 and chemical studies of minerals, and it may provide important information on the minerals
54 growth history and geological conditions during mineral formation. Compositional zoning,
55 involving the variations in both trace and major elements, is most suitable for studying the
56 dynamics of crystal growth (Tracy 1982). Different types of compositional zoning in
57 dolomite, including concentric zoning, sector zoning and oscillatory zoning, were studied
58 through imaging techniques such as cathodoluminescence (CL), back scattered electron
59 imaging (BSE) and X-ray topographs in some sedimentary rocks (e.g., Farr 1989; Reeder and
60 Prosky 1986; Reeder 1991; Wogelius et al. 1992; Shore and Fowler 1996). However, to our
61 knowledge the compositional zoning of eclogite-facies dolomite has not been reported and

3

62 thermodynamically modeled yet. Nonetheless it was rarely observed in other metamorphic
63 carbonates (*cf.*, Jones and Ghent 1971; Reinecke et al. 2000).

64 In the present study, we present concentric Fe–Mg zoning of dolomite from HP lawsonite-
65 carbonate-bearing eclogites in the southwest Tianshan (U)HP/LT metamorphic belt. The
66 petrography and mineral chemistry of the dolomite and its inclusions were studied in detail
67 by means of electron microprobe and laser ablation inductively coupled plasma mass
68 spectrometry (LA–ICP–MS). Furthermore we conducted detailed textural and
69 thermodynamic modeling studies of the dolomite and its inclusions in order to shed some
70 light on the carbonate-phase formations and transitions in subducted oceanic crust.

71 **GEOLOGICAL SETTING AND PETROGRAPHY**

72 The Chinese Tianshan (U)HP/LT metamorphic belt extends for >200 km along the South
73 Tianshan suture zone separating the Yili (-Central Tianshan) block to the north and the Tarim
74 block to the south (see Fig. 1a in Li et al. 2012; Gao et al. 1998, 2011; Han et al. 2011). It
75 mainly consists of blueschist-, eclogite- and greenschist-facies meta-sedimentary and some
76 mafic metavolcanic rocks, the latter of which have N-MORB, E-MORB, OIB and arc basalt
77 affinities (Gao et al. 1999; Gao and Klemd 2003; John et al. 2008). Peak metamorphism of
78 some eclogites was estimated to have occurred under high-pressure conditions between 14
79 and 23 kbar at 480 and 580°C (e.g., Gao et al. 1999; Klemd et al. 2002; Wei et al. 2003; Li et
80 al. 2012), while coesite relicts were identified in other eclogites or eclogite-facies rocks
81 indicating that these rocks underwent UHP metamorphism (e.g., Lü et al. 2008, 2009; Lü and
82 Zhang 2012). The intimate interlayering of HP and UHP rocks on a meter scale (Lü et al.
83 2009) was interpreted to be due to juxtaposition processes during subduction and exhumation
84 in the subduction channel (Klemd et al. 2011). The timing of peak metamorphism was
85 determined by multi-point Lu–Hf isochron ages from four blueschist- or eclogite-facies rocks

86 yielding consistent garnet-growth ages of *ca.* 315 Ma (Klemd et al. 2011). This age is in
87 agreement, within error, with U–Pb SIMS ages of *ca.* 320 Ma on metamorphic zircon rims
88 from eclogites (Su et al. 2010). White mica ^{40}Ar – ^{39}Ar and Rb–Sr ages of eclogite-facies
89 metavolcanic rocks and omphacite-bearing blueschists cluster at *ca.* 311 Ma and were found
90 to represent a major post-eclogite-facies episode of cooling or recrystallization (Klemd et al.
91 2005).

92 Marbles and carbonate-bearing HP metabasalts, metapelites are commonly observed in the
93 Tianshan (U)HP/LT metamorphic belt. The occurrence of magnesite and calcite inclusions in
94 dolomite in eclogites and metapelites was considered as evidence for UHP metamorphism
95 (Zhang et al. 2002, 2003), but the petrological interpretation of carbonate/silicate mineral
96 assemblages in (U)HP rocks is often highly controversial due to disequilibrium,
97 crystallographical or textural considerations (e.g., Klemd et al. 1994; Klemd 2003; Smit et al.
98 2008; Hammouda et al. 2011). More recently, interlayered dolomite- and magnesite-bearing
99 eclogite and blueschist in the Tianshan were interpreted to have coexisted at the same peak
100 metamorphic HP conditions due to different bulk-rock compositions (Li et al. 2012).

101 This study focuses on the chemical zoning of dolomite from a previously described HP
102 carbonate-lawsonite-bearing eclogite (sample L0910, Li et al. 2013). The peak metamorphic
103 *P–T* conditions of the eclogite are estimated at 580–590 °C and 2.2–2.4 GPa. The eclogite
104 consists of garnet (*ca.* 16 vol.%), omphacite (*ca.* 45%), carbonate (*ca.* 13%), white mica (*ca.*
105 13%), epidote (*ca.* 5%), glaucophane (*ca.* 3%), sulfide (*ca.* 2%), quartz (*ca.* 1%) and
106 accessory minerals such as rutile, titanite, lawsonite and apatite. Porphyroblastic garnet
107 contains barroisite/glaucophane, epidote, paragonite, quartz and albite in the core domain and
108 omphacite, dolomite/magnesite and rutile in the mantle domain while the rim domain usually
109 is inclusion-free. Occasionally, lawsonite and magnesite were found to be enclosed by
110 dolomite inclusions in garnet porphyroblasts. Omphacite is often orientated parallel to the

111 weak foliation as defined by phengite. Furthermore, some glaucophane inclusions were
112 detected in the omphacite cores. Significantly, the eclogite contains *ca.* 13 vol.% carbonates,
113 mainly dolomite and minor magnesite and calcite (Table 1). The dolomite occurs as
114 idioblastic/subidioblastic coarse-grained porphyroblastic matrix mineral and as inclusion in
115 garnet (Fig. 1). The matrix dolomite (0.2–1 mm in diameter) contains inclusions of omphacite,
116 glaucophane, lawsonite, phengite, paragonite, epidote, allanite, chlorite, calcite, magnesite
117 and quartz (Fig. 1), while dolomite inclusions in garnet contain magnesite, paragonite and
118 lawsonite inclusions (Fig. 1a–b; *cf.*, Li et al. 2013). Magnesite occurs as inclusion in matrix
119 dolomite and in dolomite inclusions in garnet (Fig. 1a–c). Calcite intergrown with chlorite,
120 phengite and paragonite occurs in the core of idioblastic matrix dolomite only (Fig. 1d).
121 Magnesite occasionally contains glaucophane inclusions (Fig. 1c). Epidote, which usually has
122 an allanite core, occurs as matrix mineral and as inclusion in dolomite porphyroblasts (Fig. 1d
123 and f). Lawsonite and its pseudomorphs (epidote-paragonite assemblages) were also
124 identified as inclusions in matrix dolomite (Fig. 1g).

125

ANALYTICAL METHODS

126 *In situ* major element compositions of carbonates and inclusion minerals were obtained
127 from polished thin sections by electron microprobe analysis (JEOL JXA 8200) at the
128 GeoZentrum Nordbayern (GZN) of the University Erlangen–Nürnberg, Erlangen, Germany.
129 Quantitative major element analyses were performed with an acceleration voltage of 15 kV, a
130 beam current of 15 nA, a beam diameter of 3 μm and 10–30s counting time, while qualitative
131 mapping of Ca, Fe, Mg and Mn in dolomite was conducted using an energy-dispersive X-ray
132 detector with an acceleration voltage of 15 kV, a beam current of 230 nA, a 3–5 μm pixel size
133 and dwell time of 100 ms. Natural minerals and synthetic oxides were used as standards, and
134 a program based on the ZAF procedure was used for data correction. Representative

135 microprobe analyses for the minerals in this study are presented in Table 1. In order to
136 determine the nature of the CaCO₃ polymorph occurring as inclusions in dolomite and garnet,
137 Laser-Raman spectroscopy was performed at Department of material in the same university.
138 The laser beam (wavelength of 533 nm) was focused on the CaCO₃ inclusions by means of
139 50× objectives of a polarizing microscope. The laser spot size was focused to 1 μm.

140 *In situ* trace element analyses of zoned dolomite and inclusions were performed by LA–
141 ICP–MS at the GZN using a single collector quadrupole Agilent 7500i ICP–MS equipped
142 with an UP193Fx Argon Fluoride New Wave Research Excimer laser ablation system. The
143 glass reference material NIST SRM 612 was used as standard for external calibration. LA–
144 ICP–MS measurements were conducted using a spot size of 25 μm in diameter, a laser
145 frequency of 15 Hz and 0.63 GW/cm² and a fluence of 3.32 J/cm². The carrier gas consists of
146 a mixture of 0.65 l/min helium and 1.10 l/min argon. Acquisition time was 20 s for the
147 background and 25 s for the mineral analysis. The Ca-content of the carbonates determined
148 by EMP analysis was used as internal standard. Reproducibility and accuracy, which were
149 determined for NIST SRM 610, are usually <8% and <6%. The trace element concentrations
150 were calculated by GLITTER Version 3 (van Achterbergh et al. 2000). Representative trace
151 element analyses of the carbonate minerals are given in Table 2.

152 **MINERAL CHEMISTRY**

153 Garnet has a prograde compositional growth zoning with a continuous increase of the
154 pyrope component from 4.9 to 11.4 % and a decrease of the spessartine component from 4.2
155 to 1.6 % from the core towards the rim (Table 1). Omphacite inclusions in garnet and
156 dolomite and matrix omphacite have a similar jadeite component of between 32.8 mol.% and
157 46.5 mol.%. The Si-content of phengite is between 3.45–3.51 pfu and the Na-content of
158 paragonite at *ca.* 0.80 pfu (Table 1). The glaucophane and epidote-group minerals display

159 rather uniform compositions either as matrix or inclusion minerals (Table 1). For more
160 detailed microprobe data concerning the silicates in the eclogite see Li et al. (2013).

161 The dolomite studied here is a dolomite-ankerite solid solution (dolomite_{s.s.}) that contains
162 20–35 mol.% ankerite [CaFe(CO₃)₂] component due to the substitution of Fe²⁺ for Mg (Table
163 1). This type of dolomite always contains small but variable amounts of Mn and less
164 commonly minor Sr, Pb, Ni and Zn (Table 2). LA-ICP-MS data show that the dolomite
165 contains high amounts of transition metal elements (e.g., Co: 18–60 ppm; Ni: 54–264 ppm
166 and Zn: 114–147 ppm), Sr (449–1633 ppm), Pb (2.17–27.8 ppm), P (23–28 ppm) and minor
167 Li, Ba, REE and Y (Table 2). The magnesite inclusions in the dolomite are magnesite-siderite
168 solid solutions (magnesite_{s.s.}) with a high siderite [FeCO₃] component (44–47 mol.%) and
169 about 1 mol.% CaCO₃ and even less MnCO₃ (Table 1). Magnesite hosts higher amounts of
170 transition metal elements (e.g., Co: 127–252 ppm; Ni: 181–533 ppm and Zn: 161–449 ppm)
171 but much lower Sr (0.110–5.17 ppm), Pb, HREE and Y concentrations than the dolomite
172 (Table 2). The HFSE concentrations in dolomite and magnesite are always below the
173 detection limit (Table 2). The CaCO₃ phase occurring as inclusions in dolomite is calcite
174 according to Raman spectrometry (Fig. 1d) and contains minor Mg, Fe and Mn contents
175 (Table 1). However, the stability of aragonite instead of calcite at HP/LT metamorphic
176 conditions is suggested by the thermodynamic modeling (see below) which is in agreement
177 with experimental studies (*cf.*, Carlson 1980). Thus, the calcite inclusions are thought to have
178 formed at the expense of former aragonite at low-*P* and high-*T* during post peak metamorphic
179 conditions (e.g., Carlson 1980; Proyer et al. 2008).

180

181 **COMPOSITIONAL ZONING OF DOLOMITE**

182 **Major elements**

183 The zoning of dolomite is petrographically displayed by a change in color from core to rim
184 in the BSE images (here displayed by changes of the gray intensity, Fig. 1d). The dolomite
185 core contains inclusions of calcite (probably after aragonite), magnesite_{s.s.}, phengite,
186 paragonite, epidote, lawsonite, epidote and paragonite intergrowth (possibly after lawsonite)
187 and occasionally omphacite. Omphacite, phengite and allanite inclusions occur in the darker
188 rim domains (Fig. 1d and f). The Ca content of dolomite is rather homogeneous with a slight
189 increase at the outer-rim (Figs. 2 and 3a). The Fe content continuously decreases from core
190 (12.66 wt.%) to rim (7.51 wt.%) while the Mg content increases from 13.29 wt.% to 16.97
191 wt.% (Table 1). Thus X_{Fe} ($=Fe/(Fe+Mg)$) decreases accordingly (Fig. 3a). The Mn content
192 decreases from the dolomite core (0.53 wt.%) towards the inner-rim (0.18 wt.%) while it
193 increases at the outermost rim (0.40 wt.%). In addition, a subtle oscillatory Mn zoning occurs
194 in the inner-rim domain (Fig. 2). Magnesium and Fe show a good negative correlation in the
195 Mg vs. Fe plot (Fig. 3b). Interestingly, Mn shows a negative correlation with Mg and a
196 positive correlation with Fe when neglecting the outer-rim Mn composition (Fig. 3c–d). The
197 large scale mapping images document that the dolomite inclusions in garnet and matrix
198 dolomite grains share the same compositional core-to-rim zoning pattern; however, the
199 dolomite inclusions in garnet lack the (mantle-) rim domain in contrast to the matrix dolomite
200 (Fig. 4).

201

202 **Trace elements**

203 The Sr and Pb concentrations decrease gradually from the dolomite core to the mantle and
204 increase from the mantle to the inner-rim with an abrupt decrease at the outer-rim (Fig. 5a).
205 Lithium, Ba and Sr display similar distribution patterns throughout the zoning profile (Fig.
206 5a). Manganese and Co exhibit a general decrease from core to rim and a slight oscillatory
207 zoning at the inner-rim and an increase at the outermost rim (Fig. 5b). Zinc displays a flat

208 pattern. Vanadium, Cr and Ni concentrations decrease from core to mantle and then increase
209 towards the rim with a significant drop at the outermost rim (Fig. 5b). In general, the
210 dolomite core contains higher REE and Y concentrations than the mantle and rim (Fig. 5c and
211 d). The chondrite-normalized REE diagram displays a MREE (especially Eu) enrichment
212 relative to the LREE and HREE (Fig. 5d). The REE patterns presented here are in accordance
213 with those of dolomite from other Tianshan eclogites (van der Straaten et al. 2008) but are
214 quite different with the flat REE patterns in dolomite from Central Dabie coesite-bearing
215 eclogites (Sassi et al. 2000). This discrepancy is believed to be due to different chemical bulk
216 compositions of the protoliths (e.g. oceanic crust vs. continental crust) and/or the different
217 rock mineralogy, which strongly controls the trace element distributions. The magnesite
218 shows a relative HREE enrichment compared to the LREE and MREE (Fig. 5e).

219

220

THERMODYNAMIC MODELING

221 In order to obtain information on the carbonate-phase transitions as well as compositional
222 variation of carbonates during HP/LT metamorphism, thermodynamic modeling of the
223 carbonate-bearing eclogite L0910 was undertaken in the NMnCaKFMASCHO (Na₂O–MnO–
224 CaO–K₂O–FeO–MgO–Al₂O₃–SiO₂–CO₂–H₂O–Fe₂O₃) model system using the Perple_X
225 software (Connolly 1990, 2005) and an internally consistent thermodynamic dataset (Holland
226 and Powell 1998; and update) based on the effective bulk-rock composition (Table 3).
227 Mineral solid-solution models are *Gt(WPH)* for garnet (White et al. 2007), *Omph(GHP)* for
228 omphacite (Green et al. 2007), *Amph(DPW)* for amphibole (Dale et al. 2005), *Mica(CHA)* for
229 phengite (Coggon and Holland 2002), *Chl(HP)* for chlorite (Holland and Powell 1998),
230 *Ep(HP)* for epidote (Holland and Powell 1998), and *F* for H₂O–CO₂ fluid solution (Connolly
231 and Trommsdorff 1991). In particular, the recently developed solid-solution model

10

232 *odCcMS(EF)* for ternary Ca–Fe–Mg carbonates (Franzolin et al. 2011) was used to determine
233 compositional variations in dolomite, the transition of carbonate minerals and the effect of Fe
234 on carbonate stabilities during subduction conditions. For more details concerning the
235 pseudosection calculations see Li et al. (2013).

236 A calculated phase equilibrium diagram is presented in Figure 6a. Omphacite, phengite and
237 garnet are stable phases over the whole shown P – T range, while lawsonite occurs in the low–
238 T range from which epidote-group minerals are absent. Amphibole is absent in the HT/HP
239 stability fields. Dolomite is stable over a wide P – T range, while magnesite occurs in the
240 higher-pressure and aragonite in the LP/LT fields only (Fig. 6b). The modal amounts of
241 dolomite, aragonite, magnesite, chlorite, amphibole, omphacite, lawsonite and garnet, along
242 with the X_{Fe} isopleths of magnesite_{s.s.} and dolomite_{s.s.} were contoured in the modeled
243 pseudosection (Fig. 6). The modal amount of dolomite increases and that of aragonite
244 decreases with increasing P and T in the aragonite-dolomite transition area (Fig. 6a). The
245 modal amount of magnesite decreases and that of dolomite increases with increasing T in the
246 magnesite-bearing P – T range of 550 to 600°C (Fig.6a). The X_{Fe} isopleths of magnesite_{s.s.} are
247 parallel to the P -axis and decrease in value from low to high temperatures in the amphibole-
248 absence field (Fig. 6b). Similarly, the X_{Fe} isopleths of dolomite_{s.s.} are parallel to those of
249 magnesite and also decrease from low to high temperatures in this field (Fig. 6b). The
250 chemical changes as displayed by the X_{Fe} contents of the dolomite_{s.s.} are in agreement with
251 the compositional variations observed in the zoned dolomite in the lawsonite-bearing eclogite
252 (Figs. 2 and 3a). The P – T paths of the studied eclogite and nearby eclogites (*cf.*, Li et al. 2012,
253 2013) indicate that the low temperature/low pressure aragonite was progradely transformed to
254 dolomite_{s.s.} and then to dolomite_{s.s.} and magnesite_{s.s.} during increasing P – T conditions (Fig. 6b,
255 Table 3). The modal amount of omphacite (and of dolomite_{s.s.} and magnesite_{s.s.}) increases at
256 the expense of chlorite and amphibole with increasing P – T conditions (Fig. 6b–d). Garnet

257 growth at the expense of lawsonite started at temperatures between 550 and 600°C (Fig. 6f
258 and g).

259

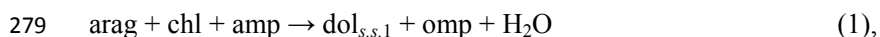
260

DISCUSSION

261 **Formation of dolomite and its prograde compositional zoning**

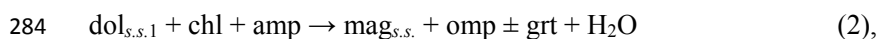
262 Significant amounts of carbonates are introduced into mafic oceanic crust by hydrothermal
263 alteration prior to subduction (e.g., Staudigel 2003). The crystallographically-bound CO₂ that
264 preferentially occurs in carbonates in the slab rocks is carried down to great mantle depths
265 without prominent decarbonation (Kerrick and Connolly 2001). Dolomitic carbonates are
266 generally stable at pressures of up to 2–7 GPa in mafic eclogites (e.g., Yaxley and Green
267 1994; Molina and Poli 2000; Poli et al. 2009). High-pressure experimental data on the
268 carbonate stability based on a basaltic composition in the presence of a H₂O–CO₂ mixed fluid
269 demonstrate that calcite is stable at $P \leq 1.4$ GPa, dolomite at P between 1.4 and 1.8 GPa, and
270 dolomite and magnesite at $P \geq 1.8$ GPa (Molina and Poli 2000). These results are in
271 accordance with the presented modeling which suggests the stability of aragonite at $T \leq$
272 450°C, $P \leq 1.7$ GPa, of dolomite at $1.7 \leq P \leq 2.1$ GPa and of dolomite and magnesite at even
273 higher pressures (e.g., $P \geq 2.1$ GPa) (Fig. 6).

274 The occurrence of calcite (after aragonite)-chlorite inclusions in dolomite core domains in
275 the studied sample (Fig. 1d) and calcite (after aragonite)-chlorite-dolomite inclusions in
276 garnet cores (Fig. 1h) in adjacent eclogite (*cf.*, Li et al. 2012) suggest the prograde formation
277 of dolomite at LT–LP conditions ($400 \leq T \leq 480^\circ\text{C}$, $1.5 \leq P \leq 2.1$ GPa) according to the
278 continuous reaction:



280 this reaction corresponds to a decrease in the modal amounts of aragonite, chlorite and

281 amphibole and an increase of dolomite and omphacite in the pseudosection (see hatched area
282 A; Fig. 6a and c–e). During increasing P – T conditions dolomite partly reacts to magnesite
283 (hatched area B) according to the reaction:



285 this reaction is displayed by increasing modal amounts of magnesite and omphacite (and
286 garnet) which formed at the expense of chlorite and amphibole along the P – T path (hatched
287 area B in the pseudosection, Fig. 6a–e). This is supported by glaucophane inclusions in
288 magnesite (Fig. 2c). The lawsonite and magnesite_{s,s} inclusions in matrix dolomite (Figs. 1c
289 and g) and in dolomite inclusions in garnet (*cf.*, Li et al. 2013) suggest that with increasing
290 temperatures and pressures dolomite formed at the expense of magnesite (e.g., $550 \leq T \leq$
291 600°C , $P \geq 2.1$ GPa) according to the continuous reaction:



293 corresponding with gradually decreasing modal abundances of magnesite and lawsonite (Fig.
294 6a and f) and increasing modal amounts of dolomite and garnet (Fig. 6a and g) in the
295 pseudosection (hatched area C; Fig. 6b). The change in the modeled chemical composition
296 (X_{Fe}) of the dolomite (Fig. 6b) is in good agreement with that of the EPM-analyses of the
297 dolomite_{s,s,2} (Table 1, No. 4–8; Fig. 3a). In addition, the measured chemical composition of
298 the magnesite_{s,s} inclusions ($X_{\text{Fe}} \approx 0.47$) in dolomite (Table 1, No. 9–10) corresponds with that
299 of the modeled magnesite_{s,s} ($X_{\text{Fe}} = 0.40$ – 0.50) in the pseudosection (area B–C; Fig. 6b).

300 Chemical zoning in metamorphic minerals relates to the changing effective bulk rock
301 composition and the precipitating fluid during changing pressures and/or temperatures (e.g.,
302 Tracy 1982). In case of a closed chemical system chemical zoning is directly related to the
303 availability of reactants and the degree of reaction completion. Reaction (3) suggests that
304 dolomite and garnet formed simultaneously. The garnet in eclogite L0910 shows distinctive
305 prograde growth zoning with continuously decreasing Fe- and Mn-contents and a gradually

306 increasing Mg-content from core to rim, respectively (Li et al. 2013). X-ray maps and
307 composition profiles display that the dolomite porphyroblasts exhibit the same compositional
308 zoning as the garnets (Figs. 2 and 3a). The symmetric concentric chemical zoning occurs both
309 in matrix dolomite and dolomite inclusions in garnet (Fig. 4) suggesting that the zoning is the
310 product of prograde growth processes. This assumption is supported by the following
311 evidence: 1) the dolomite contains mineral inclusions of glaucophane, lawsonite (and its
312 pseudomorphs), chlorite, allanite, epidote, white mica and omphacite (Fig. 1) indicating that
313 the growth of dolomite may have occurred during the blueschist-facies to eclogite-facies
314 stages; 2) the thermodynamic modeling reveals that the Fe substitution of Mg in dolomite
315 decreases during the prograde P - T evolution (Fig. 6), which is in agreement with the
316 observed Fe-Mg zoning in dolomite; and 3) matrix dolomite grains and dolomite inclusions
317 in garnet have the same core (-mantle) compositional zoning pattern (Fig. 4).

318 Decreasing Fe and increasing Mg contents from core to rim of the dolomite are believed to
319 be the result of a changing matrix bulk rock composition during temperature increase as
320 revealed by the thermodynamic modeling (Fig. 6). The prograde chlorite and amphibole
321 breakdown supply the Mg for the dolomite formation and at the same time the garnet
322 crystallization reduces the Fe concentration in the system. However, the core-to-inner rim
323 Mn decrease of the dolomite is thought to be the result of fractional crystallization, which
324 was already proposed for similar zoned siderite porphyroblasts from greenschist-facies
325 phyllites of the Esplanade Range and Northern Dogtooth Mountains in British Columbia
326 (Jones and Ghent 1971). Trace element zoning of dolomite such as decreasing core-to-rim
327 concentrations of Sr, Pb, transition metal elements, REE (Fig. 5a-d) and Y (*cf.*, garnet,
328 Hollister 1966), is believed to be further evidence for fractional crystallization of the
329 dolomite. The abrupt Mn increase at the outer-rim of the dolomite accompanied by large
330 compositional changes of the Fe- and Mg-contents (Figs. 2 and 3) along with the sudden

331 variations of trace elements (Fig. 5a–c), may be attributed to variations in the equilibrium
332 fluid composition or to disequilibrium crystallization during the last porphyroblastic growth
333 stages (*cf.*, Jones and Ghent 1971).

334

335 **The occurrence of magnesite in dolomite in the Tianshan eclogites**

336 The occurrence of magnesite ± calcite (aragonite) inclusions in dolomite was interpreted as
337 evidence for UHP metamorphism in excess of 5 GPa for eclogite-facies-rocks from the
338 Tianshan orogen (Zhang et al. 2002, 2003). These authors referred to the equilibrium reaction
339 dolomite = magnesite + aragonite in order to deduce these exceptionally high UHP conditions
340 (*cf.*, Hammouda et al. 2011, and references therein). The stability of magnesite at ultrahigh
341 pressure conditions (e.g., >5GPa) was confirmed by a series of experiments (Hammouda et al.
342 2011, and references therein) and some field observations (e.g., Zhang and Liou 1994;
343 Messiga et al. 1999). On the other hand, Fe-rich magnesite_{s.s.} and dolomite_{s.s.} were
344 experimentally shown to be stable at HP as well as UHP conditions in mafic Fe-rich eclogites.
345 However, the influence of Fe on the carbonate structure and thus their stability was not
346 discussed in detail by these studies (e.g., Dasgupta et al. 2004; Yaxley and Brey 2004),
347 although recently it was experimentally shown that the Fe-content plays an decisive role in
348 effecting the ordering-disordering state of dolomite (Franzolin et al. 2012) and, thus, has a
349 considerable effect on the magnesite-aragonite-dolomite stability relationship (Hammouda et
350 al. 2011). In Fe-bearing systems, experimental results suggest that the nucleation of aragonite
351 and magnesite occurs prior to that of dolomite at relatively low-pressure/low-temperature
352 conditions. Furthermore, a relatively high Fe proportion is expected to shift the aragonite +
353 magnesite_{s.s.} ↔ dolomite reaction toward higher temperatures, enlarging the stability field of
354 aragonite and magnesite_{s.s.} (Franzolin et al. 2012). For instance, aragonite and magnesite_{s.s.}
355 are stable between 400 and 450°C at *ca.* 2 GPa and react to highly disordered dolomite only

356 at temperatures $> 450^{\circ}\text{C}$ in Fe-rich systems (see Fig. 10 in Hammouda et al. 2011). In the
357 present study, the application of a new thermodynamic solid-solution model for Ca–Mg–Fe
358 carbonate provides an opportunity to investigate the transition of carbonate minerals during
359 subduction zone metamorphism. In the modeled complex system using a particular bulk
360 chemistry (Fig. 6a) aragonite occurs in the low temperature/low pressure stability fields in the
361 phase equilibrium diagram while magnesite_{s,s} appears only at $P > 2.0$ GPa (Fig. 6) indicating
362 that Fe-rich magnesite (in equilibrium with dolomite) is stable under high-pressure conditions
363 ($P \leq 2.5$ GPa, $T \leq 600^{\circ}\text{C}$), but is expected to react out to dolomite at temperatures $> 600^{\circ}\text{C}$
364 (Fig. 6).

365 Thus, the reported magnesite_{s,s} inclusions in dolomite_{s,s,2} (Table 1) from the Tianshan HP
366 eclogites may have formed prograde in equilibrium with dolomite_{s,s,1} and not during
367 decompression as previously proposed (Zhang et al. 2003). This interpretation is also
368 supported by glaucophane inclusions in the magnesite (Fig. 1c) and the occurrence of
369 dolomite-rimmed magnesite inclusions in the core domain of prograde garnet porphyroblasts
370 (Fig. 1a–b) (see also Li et al. 2012). These textural observations indicate that Fe-magnesite
371 formed at the expense of glaucophane between 500 and 560°C at $2.0 \leq P \leq 2.3$ GPa and was
372 then transformed to dolomite prior to or simultaneously with the pervasive garnet growth
373 during increasing P – T conditions. Consequently caution is warranted in interpreting
374 magnesite occurrences in dolomite in eclogite facies rocks as unambiguous evidence for UHP
375 metamorphism (see also Smit et al. 2008). Alternatively, fluid flow along micro cracks may
376 enter the inner part of garnet (or other container minerals) and thus may change the carbonate
377 composition of inclusions forming pseudomorph after older minerals. In addition, it should be
378 kept in mind that magnesite and dolomite assemblages cannot be treated as an absolute
379 pressure indicator without a strict control of the relative amounts of volatile and non-volatile
380 components in multi-component Fe-bearing systems (Poli et al. 2009).

381

IMPLICATIONS

382 Compositionally zoning was observed in dolomite in a lawsonite-bearing eclogite from the
383 western Tianshan HP–UHP metamorphic belt. Evidence from mineral inclusions,
384 thermodynamic modeling and textures suggest the zoning formed during prograde dolomite
385 growth under HP metamorphism. To our knowledge the compositional zoning of carbonate is
386 very rare in metamorphic rocks, and this is the first report showing the possibility to retrieve
387 such a long history from high-pressure carbonates, which are generally believed to record
388 only the latest stages of the metamorphic evolution of eclogite-facies rocks. The core–to–rim
389 Mg–Fe–Mn zoning of dolomite formed contemporaneously with garnet thereby suggesting
390 that the dolomite, like garnet, also experienced fractional crystallization during the HP
391 metamorphism. Therefore more attention should be paid to the carbonates when considering
392 mineral equilibrium and effective bulk-rock composition calculations in HP–UHP carbonate-
393 bearing rocks. In addition, our findings show that the chemical zoning in dolomite is largely
394 temperature dependent and thus the analysis of major and trace elements in carbonates from
395 blueschists and eclogites may bear important thermobarometric implications.

396 The present study shows that carbonates in subducted oceanic crust may experience
397 gradual aragonite → dolomite → dolomite+magnesite transition stages during blueschist- to
398 eclogite-facies conditions. The occurrence of magnesite_{s.s.} inclusions in dolomite enclosed in
399 garnet indicates that the magnesite_{s.s.} had formed already under HP conditions. Fe content in
400 magnesite determines its stability at lower pressures. Thus, caution is warranted using
401 magnesite occurrences in eclogite-facies rocks as unambiguous evidence for UHP
402 metamorphism, in particular in a multi-component Fe-bearing system.

403

404

ACKNOWLEDGMENTS

405 This study was funded by the Deutsche Forschungsgemeinschaft (KL692/17-3) and the
406 National Natural Science Foundation of China (41025008). We are grateful to Dr. H. Brätz
407 for assistance with the LA-ICP-MS and to Dr. H.X. Bao for help with the Raman
408 measurements. Dr. T. John is thanked for discussion on various topics of the manuscript. The
409 first author thanks the DAAD for the scholarship supporting his PhD study in Germany.
410 Constructive reviews by Drs. S. Poli and H.P. Schertl are greatly appreciated. Dr. E. Ghent is
411 thanked for his comments and editorial work. This publication is a contribution to IGCP
412 Project 592.

413

REFERENCES CITED

- 414 Carlson, W.D. (1980) The calcite-aragonite equilibrium: effects of Sr substitution and anion
415 orientational disorder. *American Mineralogist*, 65, 1252–1262.
- 416 Coggon, R. and Holland, T.J.B. (2002) Mixing properties of phengitic micas and revised
417 garnet-phengite thermobarometers. *Journal of Metamorphic Geology*, 20, 683–696.
- 418 Connolly, J.A.D. (1990) Multivariable phase-diagrams: an algorithm based on generalized
419 thermodynamics. *American Journal of Science*, 290, 666–718.
- 420 ——— (2005) Computation of phase equilibria by linear programming: A tool for
421 geodynamic modelling and its application to subduction zone decarbonation. *Earth and
422 Planetary Science Letters*, 236, 524–541.
- 423 Connolly, J.A.D. and Trommsdorff, V. (1991) Petrogenetic grids for metacarbonate rocks:
424 pressure-temperature phase-diagram projection for mixed-volatile systems. *Contributions
425 to Mineralogy and Petrology*, 108, 93–105.
- 426 Dale, J., Powell, R., White, R.W., Elmer, F.L., and Holland, T.J.B. (2005) A thermodynamic
427 model for Ca-Na clin amphiboles in Na₂O-CaO-FeO-MgO-Al₂O₃-SiO₂-H₂O-O for

18

- 428 petrological calculations. *Journal of Metamorphic Geology*, 23, 771–791.
- 429 Dasgupta, R., Hirschmann, M.M., and Withers, A.C. (2004) Deep global cycling of carbon
430 constrained by the solidus of anhydrous, carbonated eclogite under upper mantle
431 conditions. *Earth and Planetary Science Letters*, 227, 73–85.
- 432 Farr, M.R. (1989) Compositional zoning characteristics of late dolomite cement in the
433 cambrian bonnetterre formation, Missouri: Implications for parent fluid migration
434 pathways. *Carbonate Evaporite*, 4, 177–194.
- 435 Franzolin, E., Schmidt, M.W., and Poli, S. (2011) Ternary Ca-Fe-Mg carbonates: subsolidus
436 phase relations at 3.5 GPa and a thermodynamic solid solution model including
437 order/disorder. *Contributions to Mineralogy and Petrology*, 161, 213–227.
- 438 Franzolin, E., Merlini, M., Poli, S., and Schmidt, M.W. (2012) The temperature and
439 compositional dependence of disordering in Fe-bearing dolomites. *American Mineralogist*,
440 97, 1676–1684.
- 441 Gao, J. and Klemd, R. (2003) Formation of HP-LT rocks and their tectonic implications in the
442 western Tianshan Orogen, NW China: geochemical and age constraints. *Lithos*, 66, 1–22.
- 443 Gao, J., Li, M.S., Xiao, X.C., Tang, Y.Q., and He, G.Q. (1998) Paleozoic tectonic evolution of
444 the Tianshan Orogen, northwestern China. *Tectonophysics* 287, 213–231.
- 445 Gao, J., Klemd, R., Zhang, L., Wang, Z., and Xiao, X. (1999) P-T path of high-pressure/low-
446 temperature rocks and tectonic implications in the western Tianshan Mountains, NW
447 China. *Journal of Metamorphic Geology*, 17, 621–636.
- 448 Gao, J., Klemd, R., Qian, Q., Zhang, X., Li, J.L., and Jiang, T. (2011) The collision between
449 the Yili and Tarim blocks of the Southwestern Altaids: Geochemical and age constraints of
450 a leucogranite dike crosscutting the HP-LT metamorphic belt in the Chinese Tianshan
451 Orogen. *Tectonophysics*, 499, 118–131.
- 452 Green, E., Holland, T., and Powell, R. (2007) An order-disorder model for omphacitic

- 453 pyroxenes in the system jadeite-diopside-hedenbergite-acmite, with applications to
454 eclogitic rocks. *American Mineralogist*, 92, 1181–1189.
- 455 Hammouda, T., Andrault, D., Koga, K., Katsura, T., and Martin, A.M. (2011) Ordering in
456 double carbonates and implications for processes at subduction zones. *Contributions to*
457 *Mineralogy and Petrology*, 161, 439–450.
- 458 Han, B.-F., He, G.-Q., Wang, X.-C., and Guo, Z.-J. (2011) Late Carboniferous collision
459 between the Tarim and Kazakhstan-Yili terranes in the western segment of the South Tian
460 Shan Orogen, Central Asia, and implications for the Northern Xinjiang, western China.
461 *Earth-Science Reviews*, 109, 74–93.
- 462 Holland, T.J.B. and Powell R. (1998) An internally consistent thermodynamic data set for
463 phases of petrological interest. *Journal of Metamorphic Geology*, 16, 309–343.
- 464 Hollister, L.S. (1966) Garnet Zoning: An Interpretation Based on the Rayleigh Fractionation
465 Model. *Science*, 154, 1647–1651.
- 466 John, T., Klemd, R., Gao, J., and Garbe-Schonberg, C.D. (2008) Trace-element mobilization
467 in slabs due to non steady-state fluid-rock interaction: Constraints from an eclogite-facies
468 transport vein in blueschist (Tianshan, China). *Lithos*, 103, 1–24.
- 469 John, T., Gussone, N., Podladchikov, Y.Y., Bebout, G.E., Dohmen, R., Halama, R., Klemd, R.,
470 Magna, T., and Seitz, H.-M. (2012) Volcanic arcs fed by rapid pulsed fluid flow through
471 subducting slabs. *Nature Geoscience*, 5, 489–492.
- 472 Jones, J.W. and Ghent, E.D. (1971) Zoned siderite porphyroblasts from the Esplanade range
473 and northern Dogtooth mountains, British Columbia. *American Mineralogist*, 56, 1910–
474 1916.
- 475 Kerrick, D.M. and Connolly, J.A.D. (2001) Metamorphic devolatilization of subducted
476 oceanic metabasalts: implications for seismicity, arc magmatism and volatile recycling.
477 *Earth and Planetary Science Letters*, 189, 19–29.

- 478 Klemm, R. (2003) Ultrahigh-pressure metamorphism in eclogites from the western Tianshan
479 high-pressure belt (Xinjiang, western China) - Comment. *American Mineralogist*, 88,
480 1153–1156.
- 481 Klemm, R., Matthes, S., and Schüssler, U. (1994) Reaction textures and fluid behaviour in
482 very high-pressure calc-silicate rocks of the Münchberg gneiss complex, Bavaria,
483 Germany. *Journal of Metamorphic Geology*, 12, 735–745.
- 484 Klemm, R., Schröter, F.C., Will, T.M., and Gao, J. (2002) P-T evolution of glaucophane-
485 omphacite bearing HP-LT rocks in the western Tianshan Orogen, NW China: new
486 evidence for 'Alpine-type' tectonics. *Journal of Metamorphic Geology*, 20, 239–254.
- 487 Klemm, R., Bröcker, M., Hacker, B.R., Gao, J., Gans, P., and Wemmer, K. (2005) New age
488 constraints on the metamorphic evolution of the high-pressure/low-temperature belt in the
489 western Tianshan mountains, NW China. *Journal of Geology*, 113, 157–168.
- 490 Klemm, R., John, T., Scherer, E.E., Rondenay, S., and Gao, J. (2011) Changes in dip of
491 subducted slabs at depth: Petrological and geochronological evidence from HP-UHP rocks
492 (Tianshan, NW-China). *Earth and Planetary Science Letters*, 310, 9–20.
- 493 Li, J.L., Klemm, R., Gao, J., and Meyer, M. (2012) Coexisting carbonate-bearing eclogite and
494 blueschist in SW Tianshan, China: petrology and phase equilibria. *Journal of Asian Earth
495 Sciences*, 60, 174–187.
- 496 Li, J.L., Gao, J., Klemm, R., John, T., and Su, W. (2013) Fluid-mediated metal transport in
497 subduction zones and its link to arc-related giant ore deposits: Constraints from a sulfide-
498 bearing HP vein in lawsonite eclogite (Tianshan, China). *Geochimica Et Cosmochimica
499 Acta*, doi: 10.1016/j.gca.2013.06.023.
- 500 Lü, Z. and Zhang, L.F. (2012) Coesite in the eclogite and schist of the Atantayi Valley,
501 southwestern Tianshan, China. *Chinese Science Bulletin*, 57, 1467–1472.
- 502 Lü, Z., Zhang, L.F., Du, J.X., and Bucher, K. (2008) Coesite inclusions in garnet from

- 503 eclogitic rocks in western Tianshan, northwest China: Convincing proof of UHP
504 metamorphism. *American Mineralogist*, 93, 1845–1850.
- 505 ——— (2009) Petrology of coesite-bearing eclogite from Habutengsu Valley, western
506 Tianshan, NW China and its tectonometamorphic implication. *Journal of Metamorphic
507 Geology*, 27, 773–787.
- 508 Messiga, B., Kienast, J.R., Rebay, G., Riccardi, M.P., and Tribuzio, R. (1999) Cr-rich
509 magnesiochloritoid eclogites from the Monviso ophiolites (Western Alps, Italy). *Journal of
510 Metamorphic Geology*, 17, 287–299.
- 511 Molina, J.F. and Poli, S. (2000) Carbonate stability and fluid composition in subducted
512 oceanic crust: an experimental study on H₂O-CO₂-bearing basalts. *Earth and Planetary
513 Science Letters*, 176, 295–310.
- 514 Poli, S., Franzolin, E., Fumagalli, P., and Crottini, A. (2009) The transport of carbon and
515 hydrogen in subducted oceanic crust: An experimental study to 5 GPa. *Earth and Planetary
516 Science Letters*, 278, 350–360.
- 517 Proyer, A., Mposkos, E., Bazicitis, I., and Hoinkes, G. (2008) Tracing high-pressure
518 metamorphism in marbles: Phase relations in high-grade aluminous calcite-dolomite
519 marbles from the Greek Rhodope massif in the system CaO-MgO-Al₂O₃-SiO₂-CO₂ and
520 indications of prior aragonite. *Lithos*, 104, 119–130.
- 521 Reeder, R.J. (1991) An overview of zoning in carbonate minerals. In C.E. Barker and O.C.
522 Kopp, Eds., *Luminescence Microscopy: Quantitative and Qualitative Aspects*. SEPM
523 Short Course Notes, 25, 77–82.
- 524 Reeder, R.J. and Prosky, J.L. (1986) Compositional sector zoning in dolomite. *Journal of
525 Sedimentary Petrology*, 56, 237–247.
- 526 Reinecke, T., Bernhardt, H.J., and Wirth, R. (2000) Compositional zoning of calcite in a high-
527 pressure metamorphic calc-schist: clues to heterogeneous grain-scale fluid distribution

- 528 during exhumation. *Contributions to Mineralogy and Petrology*, 139, 584–606.
- 529 Sassi R., Harte B., Carswell D.A., and Yujing, H. (2000) Trace element distribution in Central
530 Dabie eclogites. *Contributions to Mineralogy and Petrology*, 139, 298–315.
- 531 Schertl, H.P. and Okay, A.I. (1994) A coesite inclusion in dolomite in Dabie-Shan, China:
532 petrological and theological significance. *European Journal of Mineralogy*, 6, 995–1000.
- 533 Shore, M. and Fowler, A.D. (1996) Oscillatory zoning in minerals: A common phenomenon.
534 *Canadian Mineralogist*, 34, 1111–1126.
- 535 Smit, M.A., Bröcker, M., and Scherer, E.E. (2008) Aragonite and magnesite in eclogites from
536 the Jaeren nappe, SW Norway: disequilibrium in the system $\text{CaCO}_3\text{-MgCO}_3$ and
537 petrological implications. *Journal of Metamorphic Geology*, 26, 959–979.
- 538 Staudigel, H. (2003) Hydrothermal alteration processes in the Oceanic crust. In H. Holland
539 and K. Turekian, Eds., *Treatise on Geochemistry*, 3, 511–537
- 540 Su, W., Gao, J., Klemd, R., Li, J.L., Zhang, X., Li, X.H., Chen, N.S., and Zhang, L. (2010) U-
541 Pb zircon geochronology of Tianshan eclogites in NW China: implication for the collision
542 between the Yili and Tarim blocks of the southwestern Altaids. *European Journal of*
543 *Mineralogy*, 22, 473–478.
- 544 Sun, S.S. and McDonough, W.F. (1989) Chemical and isotopic systematics of oceanic basalts:
545 implications for mantle composition and processes. In A.D. Saunders and M.J. Norry, Eds.,
546 *Magmatism in the Ocean Basins. Geological Society Special Publication*, 42, 313–345.
- 547 Tracy, R.J. (1982) Compositional zoning and inclusions in metamorphic minerals. In J.M.
548 Ferry, Eds., *Characterization of Metamorphism Through Mineral Equilibria. Reviews in*
549 *Mineralogy and Geochemistry*, 10, 355–397.
- 550 van Achtebergh E., Ryan C. G., and Griffin W. L. (2000) GLITTER: on-line interactive data
551 reduction for the Laser Ablation ICP–MS Microprobe. Ninth Annual V. M. Goldschmidt
552 Conference, Cambridge. 7215.

- 553 van der Straaten F., Schenk V., John T., and Gao J. (2008) Blueschist-facies rehydration of
554 eclogites (Tian Shan, NW-China): Implications for fluid-rock interaction in the subduction
555 channel. *Chemical Geology*, 255, 195–219.
- 556 Wang, X.M. and Liou, J.G. (1993) Ultra-high-pressure metamorphism of carbonate rocks in
557 the Dabie Mountains, central China. *Journal of Metamorphic Geology*, 11, 575–588.
- 558 Wei, C.J., Powell, R., and Zhang, L.F. (2003) Eclogites from the south Tianshan, NW China:
559 petrological characteristic and calculated mineral equilibria in the Na₂O-CaO-FeO-MgO-
560 Al₂O₃-SiO₂-H₂O system. *Journal of Metamorphic Geology*, 21, 163–179.
- 561 White, R.W., Powell, R., and Holland, T.J.B. (2007) Progress relating to calculation of partial
562 melting equilibria for metapelites. *Journal of Metamorphic Geology*, 25, 511–527.
- 563 Wogelius, R.A., Fraser, D.G., Feltham, D.J., and Whiteman, M.I. (1992) Trace-element
564 zoning in dolomite: Proton microprobe data and thermodynamic constraints on fluid
565 compositions. *Geochimica Et Cosmochimica Acta*, 56, 319–334.
- 566 Yaxley, G.M. and Green, D.H. (1994) Experimental demonstration of refractory carbonate-
567 bearing eclogite and siliceous melt in the subduction regime. *Earth and Planetary Science*
568 *Letters*, 128, 313–325.
- 569 Yaxley, G.M. and Brey, G.P. (2004) Phase relations of carbonate-bearing eclogite assemblages
570 from 2.5 to 5.5 GPa: implications for petrogenesis of carbonatites. *Contributions to*
571 *Mineralogy and Petrology*, 146, 606–619.
- 572 Zhang, L.F., Ellis, D.J., Williams, S., and Jiang, W.B. (2002) Ultra-high pressure
573 metamorphism in western Tianshan, China: Part II. Evidence from magnesite in eclogite.
574 *American Mineralogist*, 87, 861–866.
- 575 Zhang, L., Ellis, D.J., Arculus, R.J., Jiang, W., and Wei, C. (2003) 'Forbidden zone'
576 subduction of sediments to 150 km depth - the reaction of dolomite to magnesite plus
577 aragonite in the UHPM metapelites from western Tianshan, China. *Journal of*

578 Metamorphic Geology, 21, 523–529.
579 Zhang, R.Y. and Liou, J.G. (1994) Significance of magnesite paragenesis in ultrahigh-
580 pressure metamorphic rocks. American Mineralogist, 79, 397–400.
581 ——— (1996) Coesite inclusions in dolomite from eclogite in the southern Dabie Mountains,
582 China: The significance of carbonate minerals in UHPM rocks. American Mineralogist, 81,
583 181–186.

584 **FIGURE CAPTIONS**

585 **Figure 1** Representative photomicrographs and BSE images of dolomite in carbonate-
586 lawsonite-bearing eclogite in the Tianshan (U)HP/LT metamorphic belt. All=allanite, Cal
587 =calcite, Chl=chlorite, Dol=dolomite, Ep=epidote, Gln=glaucofane, Grt=garnet,
588 Law=lawsonite, Mag_{s.s.}=magnesite-siderite_{s.s.}, Omp=omphacite, Phn=phengite,
589 Pg=paragonite, Py=pyrite, Qtz=quartz, Ttn=titanite. (a, b) Dolomite inclusions in garnet and
590 coarse-grained matrix dolomite, both enclosing Mag_{s.s.} inclusions. (c) Mag_{s.s.} inclusions in
591 dolomite containing glaucophane inclusions. (d) The zoned porphyroblastic dolomite
592 contains inclusions of calcite, chlorite, phengite, paragonite, allanite and omphacite. The
593 calcite was identified by the representative Raman shifts at 154 cm⁻¹, 279 cm⁻¹, 713 cm⁻¹ and
594 1085 cm⁻¹. (e) Glaucophane inclusions in dolomite. (f) Phengite, allanite/epidote, omphacite
595 and quartz inclusions in matrix dolomite. (g) Lawsonite inclusions and its pseudomorph
596 (epidote+paragonite assemblages) in the core domain of matrix dolomite. (h) Calcite-chlorite-
597 dolomite inclusions in garnet in nearby carbonate-bearing eclogite, see also Fig. 3d from Li et
598 al. (2012).

599 **Figure 2** X-ray intensity maps of Ca, Fe, Mg and Mn in the dolomite porphyroblast from Fig.
600 1d. The compositional zoning is displayed by core-to-rim gradually increasing Mg and
601 decreasing Fe and Mn, whereas Ca is rather homogeneous (for profile A–B see Fig. 3a). The

602 numbered circles represent LA–ICP–MS spots, the data of which are listed in Table 2.

603 **Figure 3** Chemical composition profile of the dolomite porphyroblast from Fig. 2. (a) Fe and
604 Mn decrease from core to rim while Mg increases and Ca is constant. Towards the outermost
605 rim Ca and Mn increase slightly. (b) Good negative correlation of Mg and Fe. (c, d) Mn
606 shows a negative correlation with Mg and a positive correlation with Fe, respectively.

607 **Figure 4** X-ray maps of Ca, Fe, Mg and Mn of dolomite grains from Fig. 1a–b. The dolomite
608 inclusions in garnet shows the same compositional zoning as the core (-mantle) domain of
609 matrix dolomite.

610 **Figure 5** Trace elements in the zoned matrix dolomite porphyroblast from Fig. 2 and the
611 magnesite inclusions in dolomite. (a–c) Trace element concentrations along a profile from
612 core to rim in the dolomite. (a) Li–Ba–Sr–Pb. (b) Transition metal elements. (c) REE and Y.
613 (d) Chondrite-normalized rare earth element patterns. The dolomite core contains higher REE
614 contents (especially HREE) contents than the rim. (e) Chondrite-normalized rare earth
615 element patterns of magnesite inclusions in dolomite. Normalization values are after Sun and
616 McDonough (1989).

617 **Figure 6** (a) P – T pseudosection (using *Perple_X*) in the system NMnCaKFMASCHO for the
618 eclogite based on an effective bulk composition. The pseudosection is contoured for aragonite,
619 dolomite_{s.s.} and magnesite_{s.s.} modal abundances (vol.%). (amp = amphibole; arag = aragonite;
620 chl = chlorite; dol = dolomite; ep = epidote; f = fluid; grt = garnet; law = lawsonite; mag =
621 magnesite; omp = omphacite; phn = phengite; q = quartz; rhc = rhodochrosite; zoi = zoisite).
622 For more mineral assemblages see Table 3. (b) The P – T path (for details see Li et al. 2012,
623 2013) indicates that carbonates in subducted oceanic crust undergo the aragonite → dolomite
624 → dolomite+magnesite transitions during prograde subduction zone metamorphism. The
625 pseudosections are contoured with X_{Fe} isopleths in magnesite_{s.s.} and dolomite_{s.s.}. The
626 isopleths are largely T -dependent in area C: the Fe-content decreases and the Mg-content

627 increases from low- T to high- T , which is in agreement with the measured compositional
628 zoning in eclogite-facies dolomite of this study. (c–g) The contoured modal amounts (vol.%)
629 of chlorite (c), amphibole (d), omphacite (e), lawsonite (f) and garnet (g).

Table 1

Representative major element composition of minerals in dolomite-bearing eclogite

No.	1	2	3	4	5	6	7	8	9	10	11	12	13	14	15	16	17	18	19	20	21	22	23
Mineral	Grt	Grt	Grt	Dol	Dol	Dol	Dol	Dol	Mag	Mag	Cal	Omp	Omp	Gln	Gln	Phn	Phn	Pg	Ep	Ep	All	Law	Chl
Location	core	mantle	rim	core	mantle	mantle	inner-rim	outer-rim	in Dol	in Dol	in Dol	matrix	in Dol	in Grt	in Mag	matrix	in Dol	in Dol	matrix	in Dol	in Dol	in Dol	in Dol
SiO ₂	35.01	37.64	37.33	0.01	0.02	0.00	0.02	0.01	0.01	0.00	0.07	56.69	55.87	55.68	56.53	53.06	53.52	46.83	39.20	38.88	34.20	38.82	26.18
TiO ₂	0.09	0.03	0.03	0.00	0.05	0.03	0.02	0.03	0.00	0.00	0.00	0.05	0.04	0.02	0.49	0.26	0.18	0.04	0.44	0.00	0.12	0.48	0.00
Al ₂ O ₃	23.13	21.58	21.99	0.04	0.01	0.00	0.01	0.00	0.01	0.02	0.03	10.72	10.03	11.19	10.32	26.38	25.57	39.23	26.35	28.58	20.21	30.76	18.53
Cr ₂ O ₃	0.11	0.07	0.08	0.01	0.00	0.00	0.00	0.00	0.01	0.00	0.00	0.15	0.09	0.01	0.16	0.07	0.07	0.01	0.13	0.02	0.12	0.00	0.16
FeO	29.68	29.84	27.10	12.66	11.69	10.02	9.57	7.51	34.32	33.40	1.93	7.81	9.50	12.79	11.94	2.31	3.18	0.45	8.25	5.11	11.89	0.79	29.99
MnO	1.87	1.72	0.73	0.53	0.38	0.26	0.15	0.40	0.54	1.36	0.40	0.07	0.02	0.01	0.08	0.02	0.03	0.00	0.15	0.10	0.00	0.00	0.25
MgO	1.22	2.23	2.91	13.29	14.14	15.59	15.29	16.97	21.35	20.71	0.95	5.98	5.40	8.64	9.64	3.66	3.62	0.08	0.08	0.09	0.20	0.01	13.29
CaO	8.80	7.82	9.87	27.67	28.60	28.84	28.88	30.38	0.59	0.67	59.24	10.93	9.53	1.15	0.72	0.05	0.06	1.19	22.89	23.86	17.62	17.41	0.05
Na ₂ O	0.02	0.02	0.00	0.01	0.01	0.00	0.01	0.01	0.00	0.00	0.01	8.43	9.35	7.18	7.47	0.62	0.28	6.46	0.04	0.00	0.05	0.00	0.03
K ₂ O	0.02	0.00	0.00	0.00	0.00	0.00	0.03	0.02	0.00	0.00	0.08	0.00	0.00	0.01	0.01	10.23	10.48	0.84	0.01	0.01	0.01	0.00	0.00
Total	99.95	100.95	100.05	54.22	54.90	54.74	53.98	55.33	56.83	56.16	62.71	100.83	99.83	96.68	97.20	112.66	97.00	95.16	97.53	96.65	84.45	88.27	88.48
Si	2.798	2.973	2.942	0.000	0.000	0.000	0.001	0.000	0.000	0.000	0.002	2.006	1.993	7.761	7.851	3.478	3.510	3.001	3.044	3.028	3.084	2.553	2.809
Al	2.177	2.007	2.041	0.002	0.001	0.000	0.000	0.000	0.000	0.001	0.001	0.447	0.421	1.836	1.688	2.036	1.975	2.960	2.410	2.621	2.146	2.382	2.000
Cr	0.007	0.004	0.005	0.000	0.000	0.000	0.000	0.000	0.000	0.000	0.000	0.004	0.003	0.001	0.018	0.004	0.004	0.001	0.008	0.001	0.009	0.000	0.014
Ti	0.005	0.002	0.002	0.000	0.001	0.001	0.001	0.001	0.000	0.000	0.000	0.001	0.001	0.002	0.051	0.013	0.009	0.002	0.025	0.000	0.008	0.024	0.000
Fe ³⁺	0.000	0.000	0.000	0.000	0.000	0.000	0.000	0.000	0.000	0.000	0.000	0.111	0.234	0.575	0.262	0.000	0.000	0.000	0.540	0.330	0.900	0.000	0.000
Fe ²⁺	1.984	1.971	1.786	0.349	0.316	0.267	0.258	0.194	0.931	0.920	0.048	0.120	0.050	0.915	1.125	0.127	0.174	0.024	0.000	0.000	0.000	0.043	2.691
Mn	0.127	0.115	0.049	0.015	0.010	0.007	0.004	0.011	0.015	0.038	0.010	0.002	0.001	0.001	0.009	0.001	0.002	0.000	0.010	0.007	0.000	0.000	0.023
Mg	0.145	0.263	0.342	0.654	0.680	0.740	0.735	0.784	1.032	1.017	0.042	0.315	0.287	1.795	1.996	0.358	0.354	0.008	0.009	0.010	0.027	0.001	2.125
Ca	0.754	0.662	0.833	0.979	0.989	0.984	0.998	1.008	0.021	0.024	1.892	0.414	0.364	0.172	0.107	0.004	0.004	0.082	1.905	1.991	1.703	0.000	0.006
Na	0.003	0.003	0.000	0.001	0.000	0.000	0.001	0.000	0.000	0.000	0.001	0.578	0.647	1.940	2.012	0.079	0.036	0.803	0.006	0.000	0.009	1.227	0.006
K	0.001	0.000	0.000	0.000	0.000	0.000	0.001	0.001	0.000	0.000	0.003	0.000	0.000	0.002	0.002	0.855	0.877	0.069	0.001	0.001	0.001	0.000	0.000
Cation	8	8	8	2	2	2	2	2	2	2	2	4	4	15	15	6.955	6.945	6.950	7.958	7.989	7.887	6.230	9.674
O	12	12	12	6	6	6	6	6	6	6	6	6	6	23	23	12	12	12	12.5	12.5	12.5	10	14
X _{Fe}	0.00	0.00	0.00	0.35	0.32	0.27	0.26	0.20	0.47	0.47	WEF	42.41	35.18					Ps	0.18	0.11	0.30		
Alm	66.15	65.62	59.49								JD	46.11	41.46										
Grs	24.78	21.81	27.50								AE	11.48	23.37										
Prp	4.85	8.74	11.39																				
Sps	4.22	3.83	1.62																				

(i) $X_{Fe} = Fe^{2+}/(Fe^{2+}+Mg)$; Alm: almandine, Grs: grossular, Prp: pyrope, Sps: spessartine, WEF: wollastonite+enstatite+ferrosilite, JD: jadeite, AE: aegirine, Ps: pistacite. (ii) Fe^{3+} was calculated assuming stoichiometric mineral compositions.

Table 2

Representative trace element composition (in ppm) of dolomite and magnesite. Analyses 1-15 refer to the profile in dolomite (Fig. 2 Mn).

Min. Pos. No.	Dolomite														Magnesite			
	→														rim	in matrix Dol	Dol/Gt	
	core														15	19	21	23
	1	2	3	4	5	6	7	8	9	10	11	12	13	14				
Li	2.26	2.14	2.50	2.51	1.75	2.18	2.75	1.67	1.12	1.73	2.08	5.76	4.09	5.53	2.00	<i>bdl</i>	<i>bdl</i>	<i>bdl</i>
P	28.4	27.7	24.8	26.8	26.2	22.6	25.2	28.1	22.9	27.7	30.2	25.9	25.9	28.1	23.6	26.6	28.2	13.0
Si	<i>bdl*</i>	<i>bdl</i>	<i>bdl</i>	365	<i>bdl</i>	<i>bdl</i>	<i>bdl</i>	<i>bdl</i>	433	419	<i>bdl</i>	<i>bdl</i>	<i>bdl</i>	<i>bdl</i>	<i>bdl</i>	<i>bdl</i>	723	<i>bdl</i>
Ti	<i>bdl</i>	<i>bdl</i>	<i>bdl</i>	<i>bdl</i>	<i>bdl</i>	<i>bdl</i>	<i>bdl</i>	<i>bdl</i>	<i>bdl</i>	<i>bdl</i>	<i>bdl</i>	<i>bdl</i>	<i>bdl</i>	<i>bdl</i>	<i>bdl</i>	<i>bdl</i>	<i>bdl</i>	<i>bdl</i>
V	2.35	2.13	2.17	1.87	1.88	1.63	1.98	1.65	0.950	0.940	0.865	1.33	1.41	1.77	1.17	0.664	0.973	0.401
Cr	5.29	5.16	5.33	2.92	2.45	4.73	4.12	2.96	2.17	2.22	2.93	1.71	4.11	4.57	1.50	<i>bdl</i>	3.12	1.43
Mn	3993	3646	3763	3538	3021	2824	2587	2517	2068	1916	1625	1633	1936	1232	1975	3559	5860	5293
Co	59.5	57.4	53.0	52.7	50.7	51.4	43.0	38.5	30.3	29.0	32.2	24.6	17.9	19.1	29.1	252	250	127
Ni	264	230	202	185	168	179	153	155	183	178	194	216	215	213	53.7	533	351	181
Cu	<i>bdl</i>	<i>bdl</i>	<i>bdl</i>	<i>bdl</i>	<i>bdl</i>	<i>bdl</i>	<i>bdl</i>	<i>bdl</i>	<i>bdl</i>	<i>bdl</i>	<i>bdl</i>	<i>bdl</i>	<i>bdl</i>	<i>bdl</i>	<i>bdl</i>	2.49	<i>bdl</i>	2.06
Zn	132	132	132	130	138	132	134	136	130	136	130	142	141	147	114	449	280	161
Rb	<i>bdl</i>	<i>bdl</i>	<i>bdl</i>	<i>bdl</i>	<i>bdl</i>	<i>bdl</i>	<i>bdl</i>	<i>bdl</i>	<i>bdl</i>	<i>bdl</i>	<i>bdl</i>	<i>bdl</i>	<i>bdl</i>	<i>bdl</i>	<i>bdl</i>	<i>bdl</i>	<i>bdl</i>	<i>bdl</i>
Sr	1275	1280	1344	1305	1274	1224	1274	1410	1160	1236	1531	1633	1411	1533	449	0.227	0.110	5.17
Y	10.9	6.36	4.27	1.63	1.28	0.757	0.261	0.225	0.305	0.151	0.174	0.090	0.123	0.093	0.108	0.607	0.583	0.102
Zr	<i>bdl</i>	<i>bdl</i>	<i>bdl</i>	<i>bdl</i>	15.3	<i>bdl</i>	<i>bdl</i>	<i>bdl</i>	<i>bdl</i>	<i>bdl</i>	<i>bdl</i>	<i>bdl</i>	<i>bdl</i>	<i>bdl</i>	<i>bdl</i>	1.76	<i>bdl</i>	<i>bdl</i>
Nb	<i>bdl</i>	<i>bdl</i>	<i>bdl</i>	<i>bdl</i>	<i>bdl</i>	<i>bdl</i>	<i>bdl</i>	<i>bdl</i>	<i>bdl</i>	<i>bdl</i>	<i>bdl</i>	<i>bdl</i>	<i>bdl</i>	<i>bdl</i>	<i>bdl</i>	<i>bdl</i>	<i>bdl</i>	<i>bdl</i>
Mo	0.135	0.225	0.161	0.107	<i>bdl</i>	<i>bdl</i>	<i>bdl</i>	<i>bdl</i>	0.093	<i>bdl</i>	<i>bdl</i>	0.076	0.075	<i>bdl</i>	<i>bdl</i>	0.317	0.278	0.111
Cs	<i>bdl</i>	<i>bdl</i>	<i>bdl</i>	<i>bdl</i>	<i>bdl</i>	<i>bdl</i>	<i>bdl</i>	<i>bdl</i>	<i>bdl</i>	<i>bdl</i>	<i>bdl</i>	<i>bdl</i>	<i>bdl</i>	<i>bdl</i>	<i>bdl</i>	<i>bdl</i>	<i>bdl</i>	<i>bdl</i>
Ba	1.90	1.95	2.19	1.87	2.50	1.63	1.56	1.24	0.957	0.885	1.29	1.42	0.791	1.33	0.244	<i>bdl</i>	<i>bdl</i>	0.888
La	0.316	0.252	0.239	0.100	0.121	0.317	0.138	0.163	0.154	0.126	0.146	0.248	0.117	0.144	<i>bdl</i>	0.062	<i>bdl</i>	0.084
Ce	1.05	0.690	0.733	0.330	0.385	0.738	0.397	0.301	0.498	0.486	0.481	0.750	0.349	0.338	0.049	0.224	<i>bdl</i>	0.078
Pr	0.174	0.140	0.138	0.066	0.088	0.107	0.075	0.060	0.082	0.109	0.093	0.164	0.037	0.049	0.008	0.038	<i>bdl</i>	0.013
Nd	1.31	1.06	1.08	0.493	0.375	0.787	0.258	0.619	0.679	0.429	0.687	0.972	0.349	0.364	<i>bdl</i>	<i>bdl</i>	<i>bdl</i>	<i>bdl</i>
Sm	0.711	0.687	0.661	0.266	0.326	0.259	0.149	0.171	0.347	0.253	0.346	0.326	0.169	0.122	<i>bdl</i>	<i>bdl</i>	<i>bdl</i>	<i>bdl</i>
Eu	0.596	0.458	0.473	0.483	0.442	0.381	0.375	0.348	0.236	0.226	0.220	0.256	0.171	0.182	<i>bdl</i>	<i>bdl</i>	<i>bdl</i>	<i>bdl</i>
Gd	2.14	1.40	1.29	0.445	0.721	0.447	0.156	0.153	0.417	0.206	0.229	0.297	0.072	0.089	<i>bdl</i>	<i>bdl</i>	<i>bdl</i>	<i>bdl</i>
Tb	0.381	0.256	0.208	0.086	0.068	0.066	0.019	0.014	0.032	0.020	0.009	0.028	<i>bdl</i>	0.021	<i>bdl</i>	<i>bdl</i>	<i>bdl</i>	0.009
Dy	2.39	1.66	1.14	0.410	0.287	0.249	0.104	<i>bdl</i>	<i>bdl</i>	0.047	<i>bdl</i>	<i>bdl</i>	0.049	0.056	<i>bdl</i>	<i>bdl</i>	<i>bdl</i>	<i>bdl</i>
Ho	0.418	0.257	0.135	0.080	0.043	0.028	<i>bdl</i>	<i>bdl</i>	0.011	<i>bdl</i>	<i>bdl</i>	<i>bdl</i>	<i>bdl</i>	<i>bdl</i>	<i>bdl</i>	0.045	0.031	<i>bdl</i>
Er	0.769	0.390	0.273	0.105	0.097	<i>bdl</i>	<i>bdl</i>	<i>bdl</i>	0.041	<i>bdl</i>	<i>bdl</i>	<i>bdl</i>	<i>bdl</i>	<i>bdl</i>	<i>bdl</i>	0.120	0.138	0.018
Tm	0.070	0.055	0.030	0.014	0.015	<i>bdl</i>	<i>bdl</i>	<i>bdl</i>	<i>bdl</i>	<i>bdl</i>	<i>bdl</i>	<i>bdl</i>	<i>bdl</i>	<i>bdl</i>	<i>bdl</i>	0.018	0.036	0.006
Yb	0.463	0.323	0.173	<i>bdl</i>	<i>bdl</i>	<i>bdl</i>	<i>bdl</i>	<i>bdl</i>	0.027	0.039	<i>bdl</i>	<i>bdl</i>	<i>bdl</i>	<i>bdl</i>	<i>bdl</i>	0.192	0.308	0.033
Lu	0.053	0.049	0.026	0.012	<i>bdl</i>	<i>bdl</i>	0.008	<i>bdl</i>	<i>bdl</i>	<i>bdl</i>	<i>bdl</i>	<i>bdl</i>	<i>bdl</i>	<i>bdl</i>	<i>bdl</i>	0.032	0.061	0.011
Hf	<i>bdl</i>	<i>bdl</i>	<i>bdl</i>	<i>bdl</i>	0.359	<i>bdl</i>	<i>bdl</i>	<i>bdl</i>	<i>bdl</i>	<i>bdl</i>	<i>bdl</i>	<i>bdl</i>	<i>bdl</i>	<i>bdl</i>	<i>bdl</i>	0.095	<i>bdl</i>	<i>bdl</i>
Ta	<i>bdl</i>	<i>bdl</i>	<i>bdl</i>	<i>bdl</i>	<i>bdl</i>	<i>bdl</i>	<i>bdl</i>	<i>bdl</i>	<i>bdl</i>	<i>bdl</i>	<i>bdl</i>	<i>bdl</i>	<i>bdl</i>	<i>bdl</i>	<i>bdl</i>	<i>bdl</i>	<i>bdl</i>	<i>bdl</i>
Pb	16.4	16.6	17.4	17.0	15.9	16.2	15.3	15.9	13.1	13.5	15.8	19.3	22.1	27.8	2.17	<i>bdl</i>	<i>bdl</i>	0.083
Th	<i>bdl</i>	<i>bdl</i>	<i>bdl</i>	<i>bdl</i>	0.017	0.034	0.018	<i>bdl</i>	<i>bdl</i>	<i>bdl</i>	<i>bdl</i>	<i>bdl</i>	<i>bdl</i>	<i>bdl</i>	<i>bdl</i>	<i>bdl</i>	<i>bdl</i>	<i>bdl</i>
U	<i>bdl</i>	<i>bdl</i>	<i>bdl</i>	<i>bdl</i>	0.039	<i>bdl</i>	<i>bdl</i>	<i>bdl</i>	<i>bdl</i>	<i>bdl</i>	<i>bdl</i>	<i>bdl</i>	<i>bdl</i>	<i>bdl</i>	<i>bdl</i>	0.024	<i>bdl</i>	<i>bdl</i>

**bdl*: below detection limit; Dol/Gt: magnesite in dolomite in garnet.

Tabel 3 Bulk composition used for pseudosection calculation and mineral assemblages from Fig. 6a

Sample	SiO ₂	Al ₂ O ₃	Na ₂ O	K ₂ O	FeO	Fe ₂ O ₃	MgO	CaO	MnO	CO ₂	H ₂ O
L0910	43.39	12.71	3.44	1.19	7.24	1.9	6.73	12.76	0.11	5.77	4.68

Field A:

A₁: amp omp grt phn chl arag law q f
A₂: amp omp grt phn chl dol arag law q f
A₃: amp omp grt phn chl dol arag law f

A: omp phn chl amp dol mag law rhc f
B: amp omp phn chl dol law arag rhc f
C: amp omp grt phn chl arag law ep q f
D: amp omp grt phn chl dol arag law ep q f
E: amp omp grt phn chl dol arag law ep f

Field B:

B₁: amp omp grt phn chl dol law f
B₂: omp grt amp phn chl dol mag law f
B₃: omp grt amp phn dol mag law f
B₄: omp grt amp phn dol mag law f q

F: amp omp grt phn chl arag ep q f
G: amp omp grt phn chl dol arag ep q f
H: amp omp grt phn chl dol arag ep f
I: amp omp grt phn dol law f
J: amp omp grt phn dol law ep f

Field C:

C₁: omp grt phn dol mag law q f
C₂: omp grt phn dol mag law ep q f
C₃: omp grt phn dol mag ep q f

K: amp omp grt phn dol law ep q f
L: amp omp grt phn dol mag law ep q f
M: amp omp grt phn dol mag ep q f
N: omp grt phn dol law q f
O: amp omp grt phn dol zoi q f

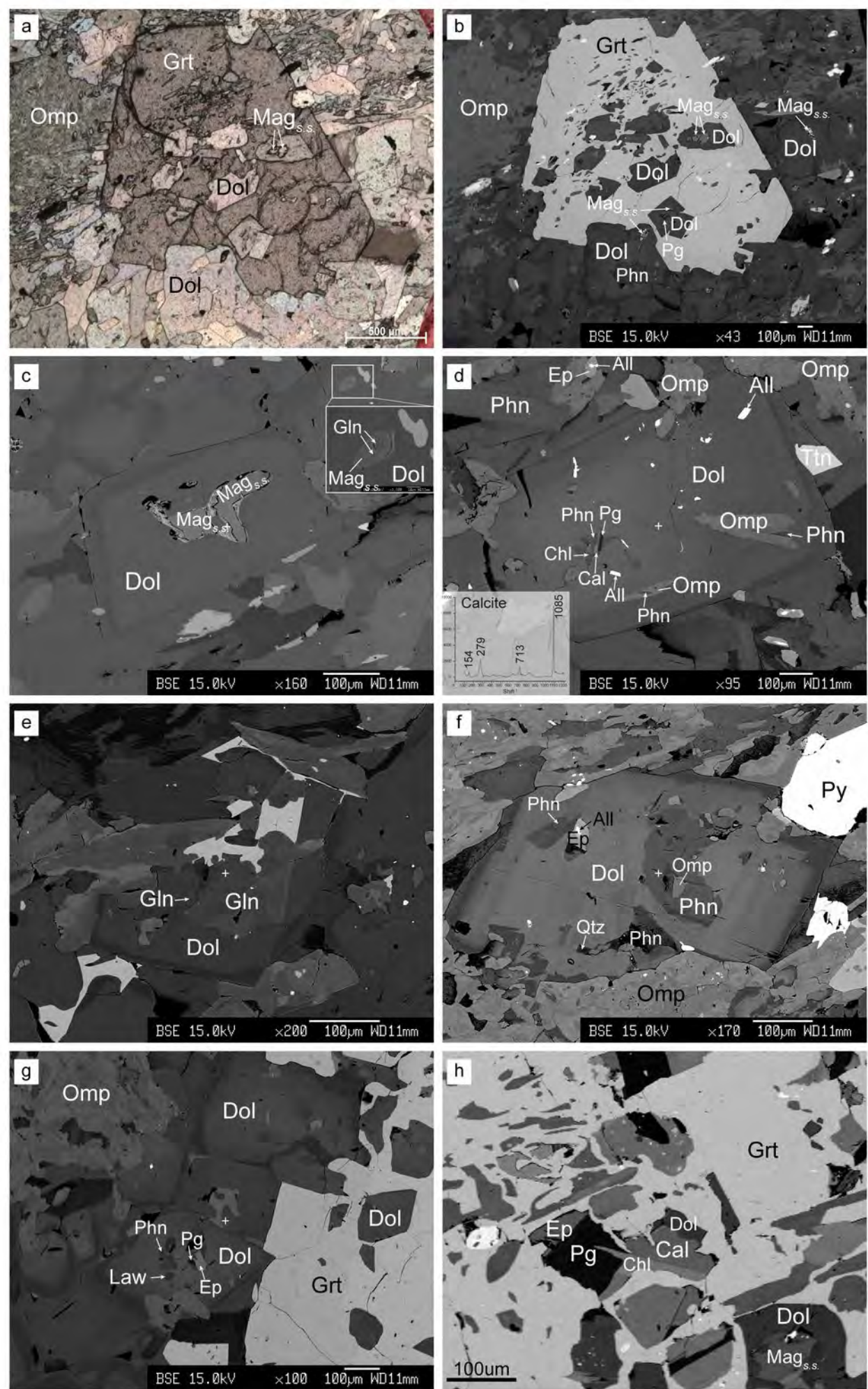


Figure 1

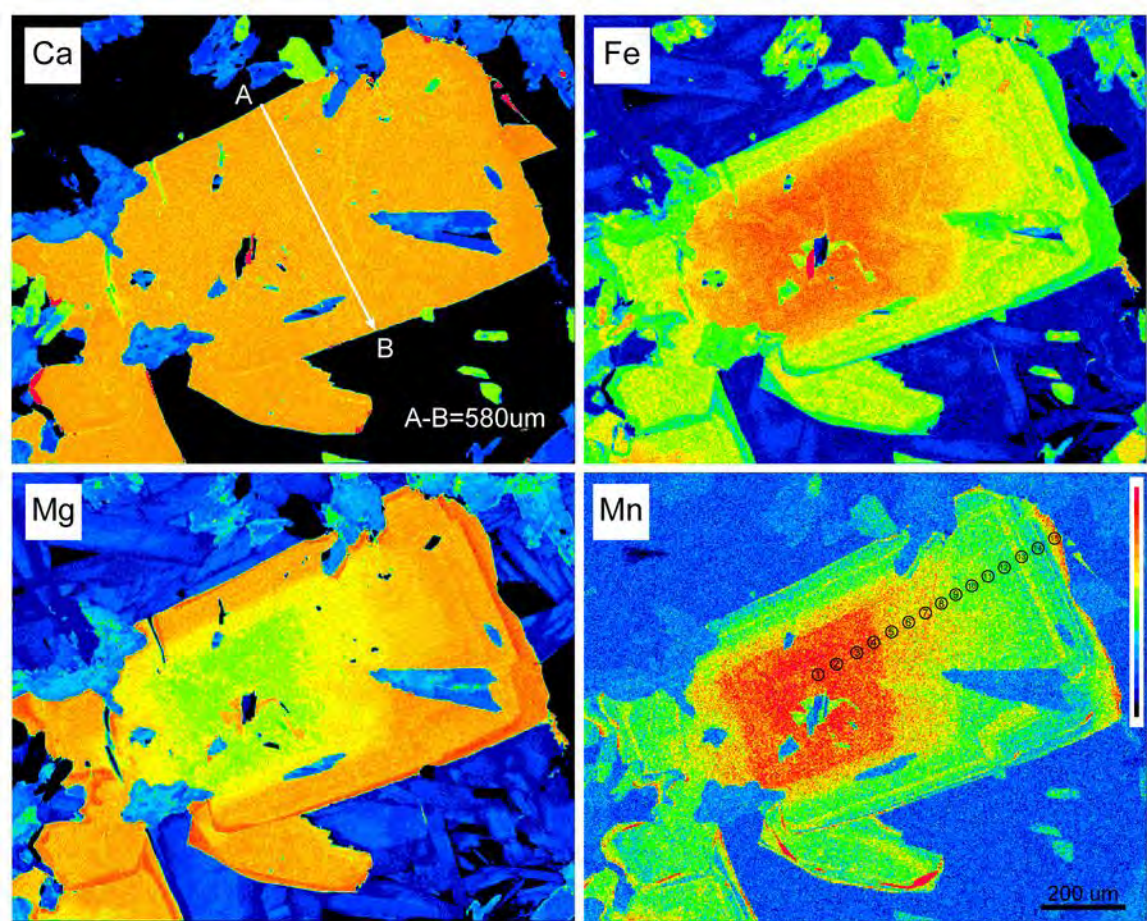


Figure 2

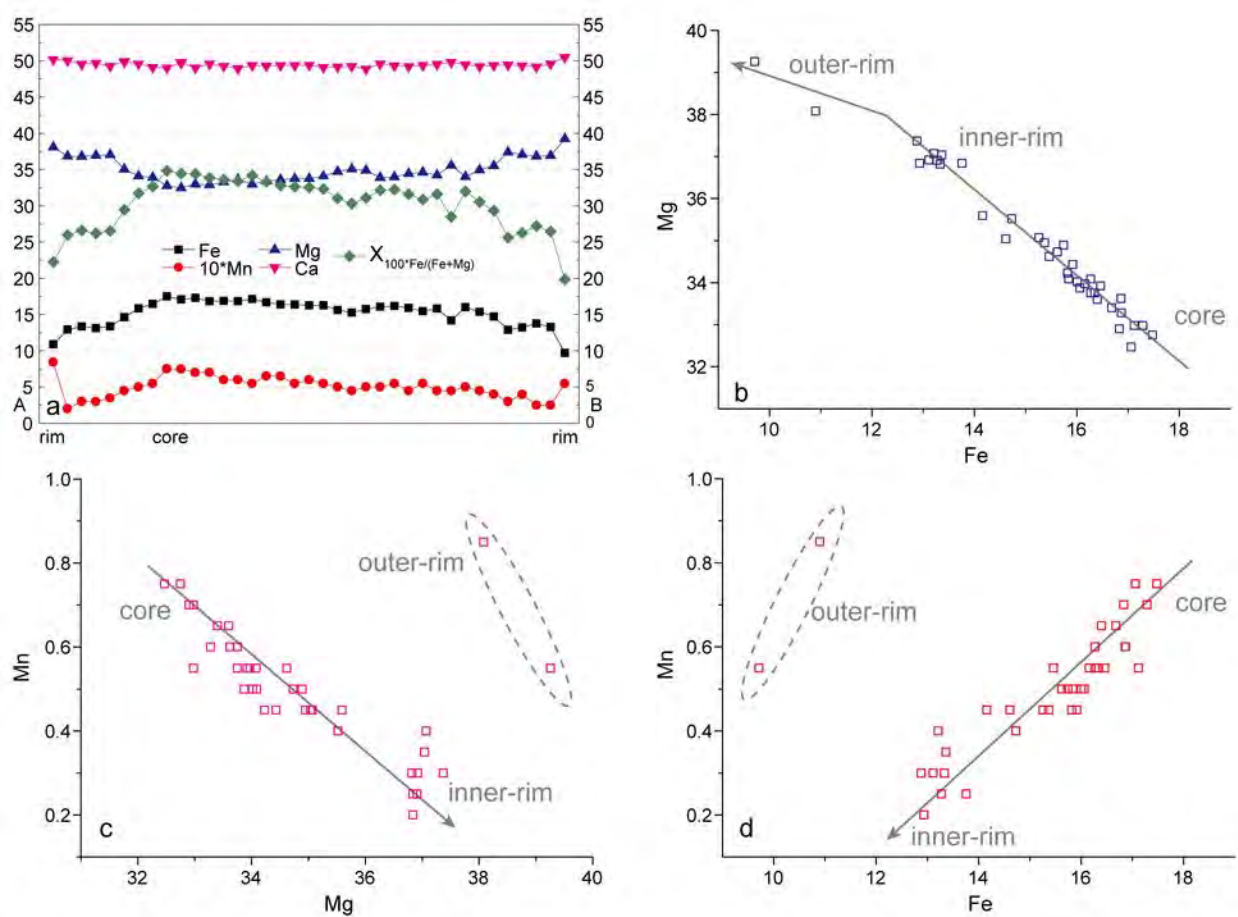


Figure 3

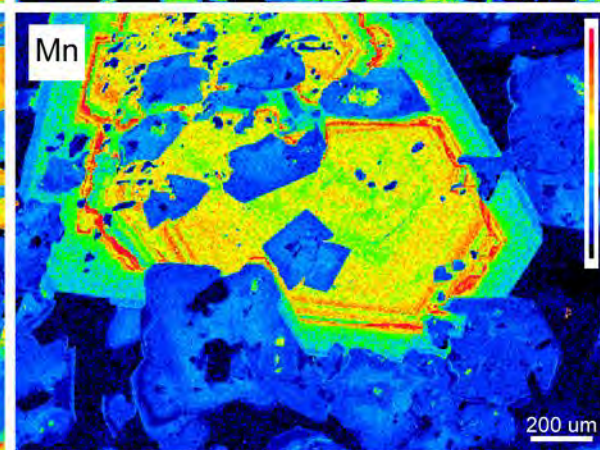
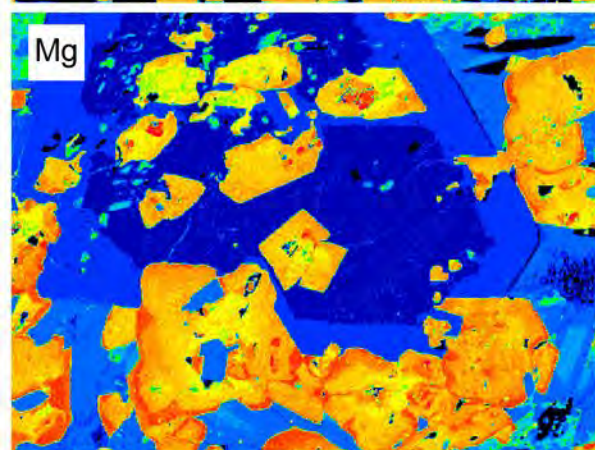
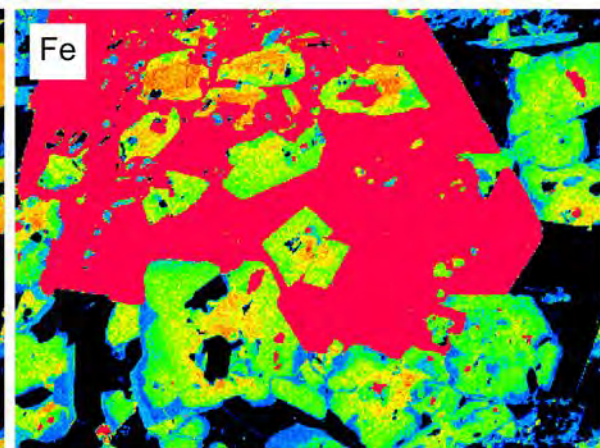
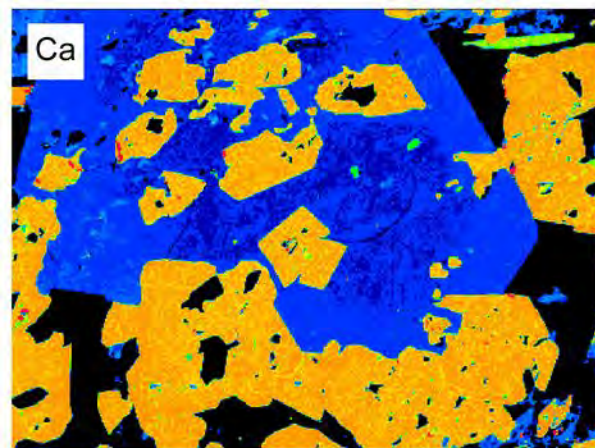


Figure 4

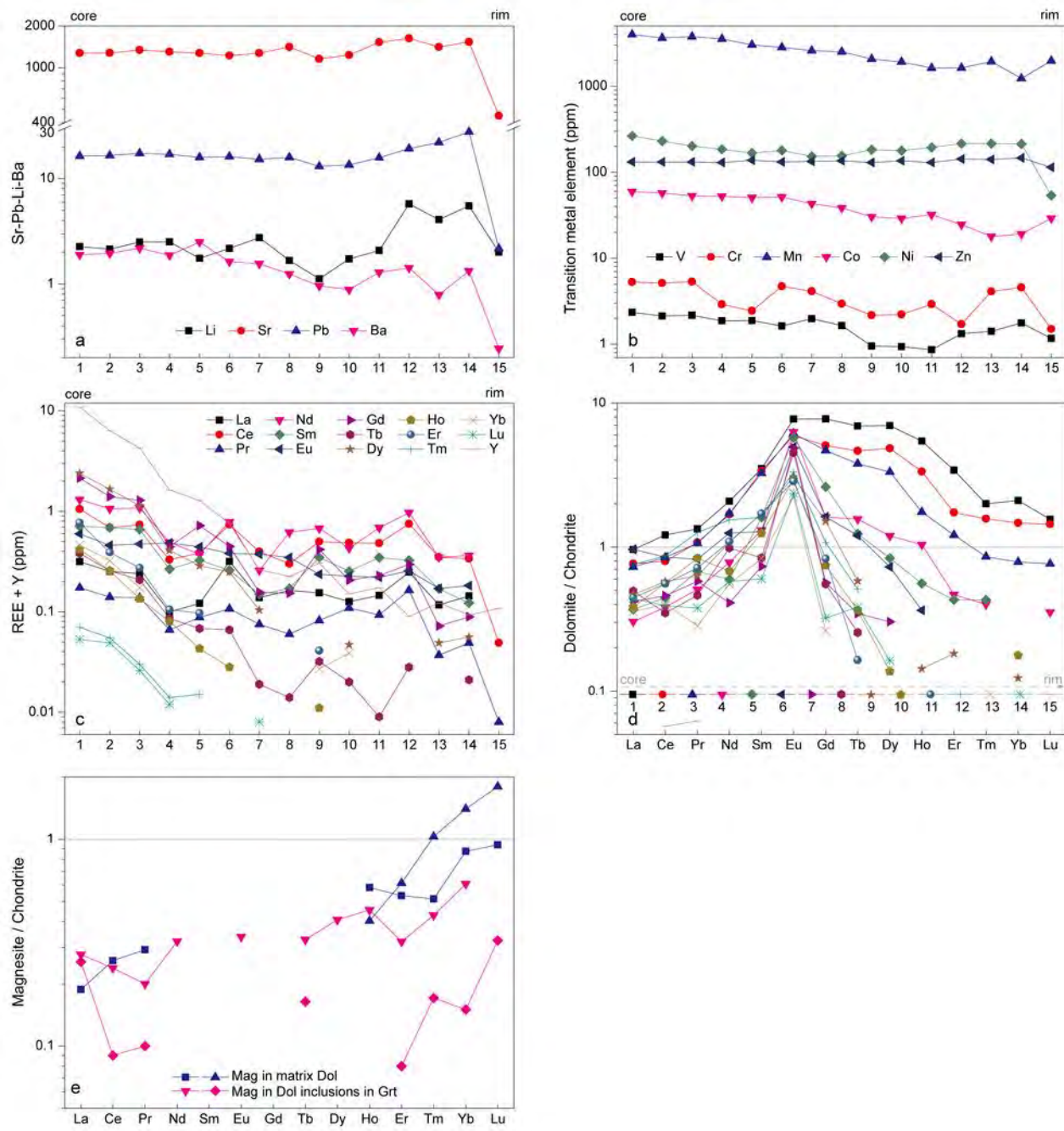


Figure 5

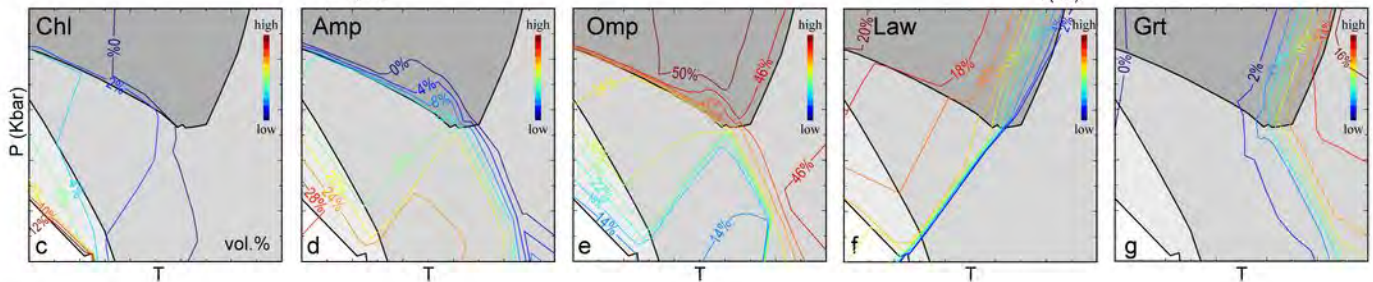
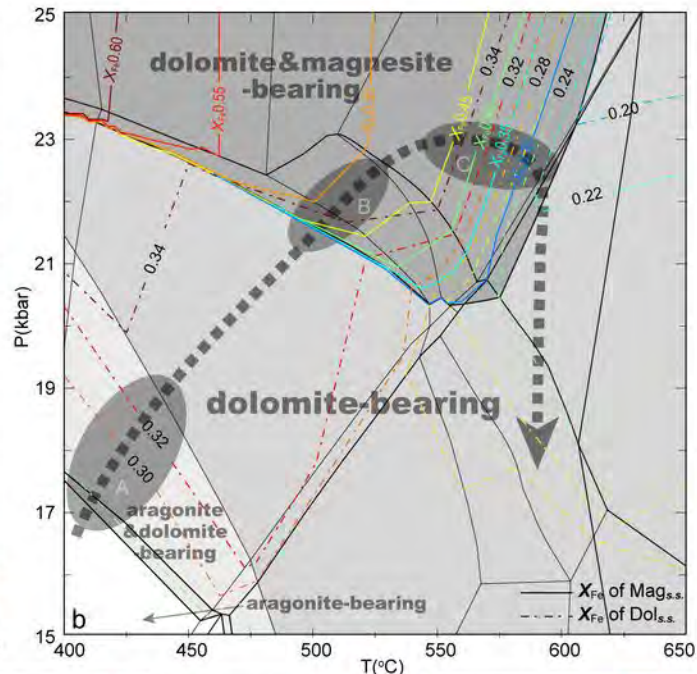
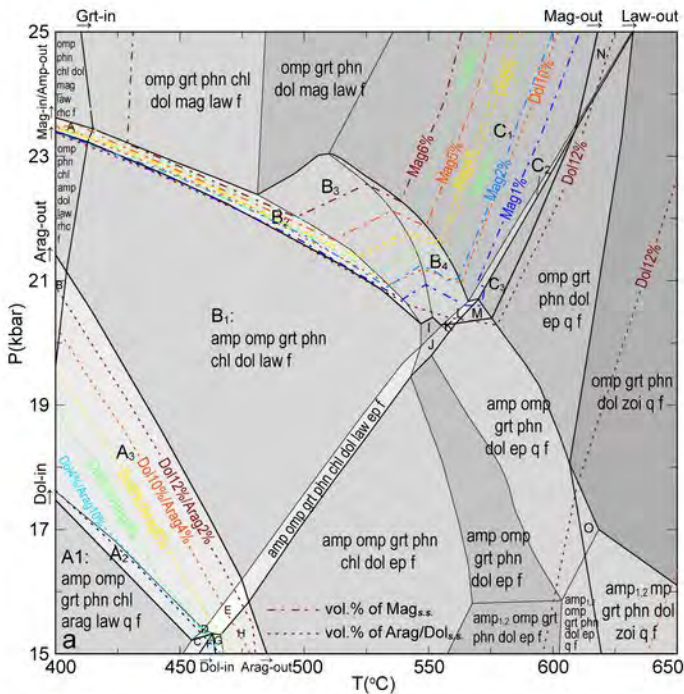


Figure 6